# Modeling the electrical conductivity in $BaTiO_3$ on the basis of first-principles calculations

Paul Erhart[1,2,a)] and Karsten Albe[2]
[1]*Chemistry, Materials, Earth, and Life Sciences Directorate, Lawrence Livermore National Laboratory, Livermore, California, 94551, USA*
[2]*Institut für Materialwissenschaft, Technische Universität Darmstadt, 64287 Darmstadt, Germany*

(Received 3 April 2008; accepted 8 May 2008; published online 28 August 2008)

The dependence of the electrical conductivity on the oxygen partial pressure is calculated for the prototypical perovskite $BaTiO_3$ based on data obtained from first-principles calculations within density functional theory. The equilibrium point defect concentrations are obtained via a self-consistent determination of the electron chemical potential. This allows one to derive charge carrier concentrations for a given temperature and chemical environment and eventually the electrical conductivity. The calculations are in excellent agreement with experimental data if an accidental acceptor dopant level of $10^{17}$ $cm^3$ is assumed. It is shown that doubly charged oxygen vacancies are accountable for the high-temperature *n*-type conduction under oxygen-poor conditions. The high-temperature *p*-type conduction observed at large oxygen pressures is due to barium vacancies and titanium-oxygen divacancies under Ti- and Ba-rich conditions, respectively. Finally, the connection between the present approach and the mass-action law approach to point defect thermodynamics is discussed. © *2008 American Institute of Physics*.
[DOI: 10.1063/1.2956327]

## I. INTRODUCTION

Point defects control the functional properties of semiconductors and many insulators, but are usually difficult to assess experimentally. If bulk properties like conductivity or diffusivity are measured, it is necessary to introduce model assumptions in order to relate the measured macroscopic quantities to microscopic point defect properties. In contrast, local probes such as electron spin resonance[1,2] or positron annihilation spectroscopy[3] can provide very specific information on point defect structures but are usually restricted to certain electronic configurations (unpaired spins) or types of defects (open volumes, vacancies). In general, only by combining several experimental probes a consistent description of the defect chemistry in a given material can be obtained.[4] To complicate things further, the correlation between defect properties and any experimentally measured response is typically indirect and often prone to ambiguities.

Computational modeling techniques evolved rapidly in recent years, in particular in the realm of first-principles calculations. Among these methods schemes based on the density-functional theory (DFT) are extremely popular as they have become increasingly reliable and have been shown to be capable of predicting various materials properties. First-principles modeling is particularly attractive with regard to point defects. It allows to obtain detailed information about thermodynamic and kinetic properties (formation energies and volumes, migration barriers and entropies) as well as the electronic structure which—at this level of detail—are not available through experimental techniques (see, e.g., Refs. 5–8). However, only in very few cases calculations of point defect properties have been employed to derive macroscopically measurable quantities such as conductivities or diffusivities (see e.g., Refs. 9 and 10). It is, however, instrumental to develop these connections between calculation and experiment in order to verify the underlying methods and to establish their predictive power.

In the present contribution we demonstrate for the case of $BaTiO_3$ how theoretical data obtained from first-principles calculations[8] can be used to derive the dependence of the electrical conductivity on the oxygen partial pressure. The electrical conductivity is a technologically highly relevant property, the understanding of which is at the very foundation of device technology. The modeling of this property described in the present paper provides the basis for future work which should address, e.g., the role of kinetic effects, extrinsic defects, or defect association.

Barium titanate is a prototypical ferroelectric material with a paraelectric-ferroelectric transition temperature of 393 K. Its most important technological application is in thin-film capacitors.[11] In addition $BaTiO_3$ serves as an end member in several lead-free ferroelectric alloys,[12] and is used—often in combination with $SrTiO_3$—to obtain tunable radio frequency devices.[13,14] Because of its technological importance it has been extensively investigated, and a reliable, as well as extensive, database is available (see, e.g., Refs. 15–23). $BaTiO_3$ is therefore not only a very interesting material for theoretical investigations, but it provides also an excellent testbed for carrying out a stringent comparison between calculated and experimental data.

In the following we first introduce the thermodynamic framework and the relevant equations of semiconductor physics. Combining these equations we are able to determine self-consistently for a given temperature and a given chemical environment: (1) the electron chemical potential, (2) the

a)Electronic mail: paul.erhart@web.de.

 

point defect concentrations, (3) the charge carrier concentrations, and eventually (4) the electrical conductivity. In Sec. III the results of the calculations are compared to high-temperature experimental data and the dependence of the conductivity on the oxygen partial pressure is analyzed in terms of the point defect equilibria in the material. The model is subsequently employed to extrapolate the materials behavior to lower temperatures, where experimental measurements are no longer available.

## II. THERMODYNAMIC FORMALISM

### A. Gibbs free energy of point defect formation

The Gibbs free energy of formation of a point defect in charge state $q$ can be consistently derived from thermodynamic principles and depends on the chemical potentials $\mu_i$ of the constituents ("the chemical environment") and the electron chemical potential $\mu_e$ as follows:[24,25]

$$\Delta G^d = (G_{\mathrm{def}} - G_{\mathrm{host}}) - \sum_j \Delta n_j \mu_j + q(E_{\mathrm{VBM}} + \mu_e), \tag{1}$$

where $G_{\mathrm{def}}$ and $G_{\mathrm{host}}$ are the Gibbs free energies of the system with and without the defect, respectively. The difference in the number of atoms of type $i$ between these two systems is denoted $\Delta n_j$ and the sum runs over the elements present in the system. It is convenient to separate the chemical potential into the chemical potential of the ground state $\mu_j^0$ and the variation relative to the ground state chemical potential $\Delta\mu_j$, i.e.,

$$\mu_j = \mu_j^0 + \Delta\mu_j. \tag{2}$$

Finally, the position of the valence band, $E_{\mathrm{VBM}}$, defines the reference of the energy scale for the electron chemical potential, $\mu_e$.

Knowledge of the defect formation energy allows one to calculate the defect concentration as a function of temperature, which is given by

$$c_i^d = c_i^0 \exp\left(-\frac{\Delta G_i^d}{k_B T}\right), \tag{3}$$

where $c_i^0$ denotes the number of sites available for defects on the respective sublattice per volume (e.g., the density of barium sites in the case of barium vacancies).

### B. Charge neutrality condition: The intrinsic electron chemical potential

The electron chemical potential $\mu_e$, which appears in Eq. (1), is actually not a free parameter but fixed by the charge neutrality condition[4]

$$n_e + n_A = n_h + n_D, \tag{4}$$

which links the concentration of intrinsic electrons $n_e$ and holes $n_h$ to the concentration of charge carriers induced by acceptors $n_A$ and donors $n_D$. As discussed in the following each term in Eq. (4) is exponentially dependent on the electron chemical potential $\mu_e$. Finding a solution of Eq. (4) therefore yields the intrinsic (self-consistent) chemical potential for a given temperature and chemical environment (Sec. II D).

The intrinsic charge carrier concentrations are obtained by integrating the number of unoccupied states up to the valence band maximum (VBM) and the number of occupied states above the conduction band minimum (CBM),

$$n_e(\mu_e) = \int_{\mathrm{CBM}}^{\infty} D(E) f(E,\mu_e) dE, \tag{5a}$$

$$n_h(\mu_e) = \int_{-\infty}^{\mathrm{VBM}} D(E)[1 - f(E,\mu_e)] dE, \tag{5b}$$

where $f(E,\mu_e) = \{1 + \exp[(E-\mu_e)/k_B T]\}^{-1}$ is the Fermi–Dirac distribution.

The concentrations of point defect induced carriers are obtained by summing the concentrations of acceptors and donors

$$n_D = \sum_i^{\mathrm{donors}} e q_i c_i^0 \exp\left(-\frac{\Delta G_i^d}{k_B T}\right), \tag{6a}$$

$$n_A = \sum_i^{\mathrm{acceptors}} e q_i c_i^0 \exp\left(-\frac{\Delta G_i^d}{k_B T}\right), \tag{6b}$$

where $e$ is the unit of charge and $q_i$ is the charge state of defect $i$. Additional charge carriers contributed by dopants or impurities ("accidental dopants") can be simply added to $n_A$ and $n_D$, respectively. Their concentrations are given by

$$n_D^{\mathrm{ext}} = e q_D c_D^{0,\mathrm{ext}} [1 - f(E_G - E_D, \mu_e)], \tag{7}$$

$$n_A^{\mathrm{ext}} = e q_A c_A^{0,\mathrm{ext}} [f(E_A, \mu_e)], \tag{8}$$

where $E_D$ and $E_A$ are the donor and acceptor equilibrium transition levels measured with respect to the CBM and the VBM, respectively, and $c_D^{0,\mathrm{ext}}$ and $c_A^{0,\mathrm{ext}}$ are the impurity concentrations.

Mathematically, it is possible that there is more than one solution of the charge neutrality condition Eq. (4). This can occur, e.g., if some defect concentrations change as a function of temperature whereas some others are held constant. In such a case the solution with the lowest Gibbs free energy is selected. The difference of the Gibbs free energy with respect to the equivalent defect-free reference system is obtained by summing the formation energies of all defects in the system minus the configurational entropy

$$\Delta G \approx \sum_i N_i \Delta G_i^d - k_B T \ln \Omega, \tag{9}$$

where $N_i$ denotes the number of defects of type $i$ and $\Omega$ denotes the number of possible configurations (compare Chap. 3.3 of Ref. 4).

### C. Electrical conductivity

The electrical conductivity is obtained by summing over all mobile charge carrying species[4]

$$\sigma = \sum_i B_i c_i q_i e, \tag{10}$$

where $B_i$ is the mobility, $c_i$ is the concentration per volume, and $q_i$ is the charge number. Typically one distinguishes the electronic and ionic contributions $\sigma = \sigma_{el} + \sigma_{ion}$. According to Eq. (10) the former is simply

$$\sigma_{el} = \underbrace{B_e n_e e}_{\text{electrons}} + \underbrace{B_h n_h e}_{\text{holes}} \tag{11}$$

where $n_e$ and $n_h$ are given by Eqs. (5a) and (5b) under the constraint that the charge neutrality condition (4) is fulfilled. Charge carrier mobilities subsume the contributions of all possible scattering mechanisms—most importantly defects and phonons—and are therefore very difficult to calculate. At present we resort to experimental data instead. For the electron mobility we use the expression given in Ref. 17 which is a fit to single crystal data from Seuter using the expression given by Ihrig,[26]

$$B_e = 8080 \frac{\text{cm}^2\ \text{K}^{3/2}}{\text{s}} T^{-3/2} \exp\left[ -\frac{0.021\ \text{eV}}{k_B T} \right]. \tag{12}$$

For the hole mobility we follow Ref. 17 and assume $B_h \approx B_e/2$.

In order to obtain the ionic conductivity one can use the Einstein–Smoluchowski relation $B_i = eD_i/k_B T$ to replace the defect mobility with the defect diffusivity $D_i = D_0 \exp(-\Delta G_i^m/k_B T)$, which yields

$$\sigma_{\text{ion}} = \sum_i \frac{q_i e^2 D_0 c_i}{k_B T} \exp\left( -\frac{\Delta G_i^m}{k_B T} \right). \tag{13}$$

For cubic crystals the prefactor is $D_0 = 6\Gamma_0 a_0^2$, where $a_0$ is the lattice constant and $\Gamma_0$ is the attempt frequency. The latter can be approximated by the lowest optical phonon frequency which yields[27] $\Gamma_0 \approx 5$ THz and $D_0 \approx 10^{-3}$ cm/s$^2$. The migration energies for intrinsic vacancies have been reported in Ref. 8. Since both the migration entropy and the migration volume are about a factor of magnitude smaller than the formation entropy and volume, they can be safely neglected in the present case, i.e., we can assume $\Delta G_i^m \approx \Delta E_i^m$. Using these data it is found that for the present material the ionic contribution at elevated temperatures is about four orders of magnitude smaller than the electronic contribution. In the following we therefore consider the electronic part only.

### D. Phase stability: Limitations on the chemical potentials

The chemical potentials $\mu_j = \mu_j^0 + \Delta\mu_j$, which appear in Eq. (1), are subject to several thermodynamic constraints. First, they cannot become more positive than the chemical potential of the reference phase, i.e., $\Delta\mu_j \leq 0$, where the reference phase for oxygen is the $O_2$ molecule, for barium the body-centered-cubic crystal, and for titanium the hexagonal-close-packed crystal. If any chemical potential reaches its upper limit, the respective elemental ground state phase precipitates. Second, the chemical potentials of the constituting elements are coupled by the requirement that[8]

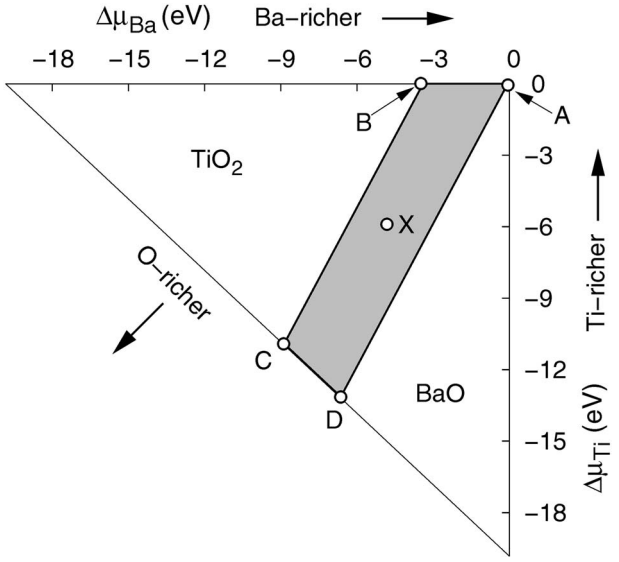


FIG. 1. Phase diagram for cubic barium titanate at 0 K as determined from density functional theory calculations (Ref. 8). The area confined between points A, B, C, and D is the chemical stability range of $BaTiO_3$. The chemical potentials confined to the lines A–D and B–C are referred to as Ba and Ti rich, respectively.

$$\Delta\mu_{\text{Ba}} + \Delta\mu_{\text{Ti}} + 3\Delta\mu_{\text{O}} = \Delta H_f[\text{BaTiO}_3], \tag{14}$$

where $\Delta H_f[\text{BaTiO}_3]$ is the formation energy of $BaTiO_3$. Further constraints result from the formation of competing phases, namely

$$\Delta\mu_{\text{Ba}} + \Delta\mu_{\text{O}} \leq \Delta H_f[\text{BaO}], \tag{15a}$$

$$\Delta\mu_{\text{Ti}} + 2\Delta\mu_{\text{O}} \leq \Delta H_f[\text{TiO}_2]. \tag{15b}$$

If all of these restrictions are included, one obtains the static phase diagram for $T = 0$ K depicted in Fig. 1. The outer triangle follows from condition (14) while the lines separating the $BaTiO_3$, $TiO_2$, and BaO phases result from Eqs. (15a) and (15b). The gray shaded area is the (0 K) stability range of $BaTiO_3$ with respect to BaO and $TiO_2$.

Experimentally, the way to control the thermodynamic boundary conditions is to use either BaO or $TiO_2$ excess during materials processing, and to vary the oxygen partial pressure, $p_{O_2}$, during processing and measurements. Adjusting the excess of either Ba or Ti corresponds to constraining the accessible range of chemical potentials to the lines A–D (Ba-rich limit, equilibrium between BaO and $BaTiO_3$) or B–C (Ti-rich limit, equilibrium between $TiO_2$ and $BaTiO_3$) in Fig. 1. Varying the oxygen partial pressure (i.e., to the oxygen chemical potential) is equivalent to moving along these lines where the extremal points A and B on one, and C and D on the other side correspond to metal-rich (low $p_{O_2}$) and oxygen-rich (high $p_{O_2}$) conditions, respectively.

While the formation energies calculated in Ref. 8 are given as a function of the chemical potentials, experimentally the conductivity is measured as a function of the oxygen partial pressure. In order to compare the conductivities as calculated for different chemical potentials with experimental data, one must therefore convert between the oxygen chemical potential and the oxygen partial pressure. The two quantities are related according to[28,29]

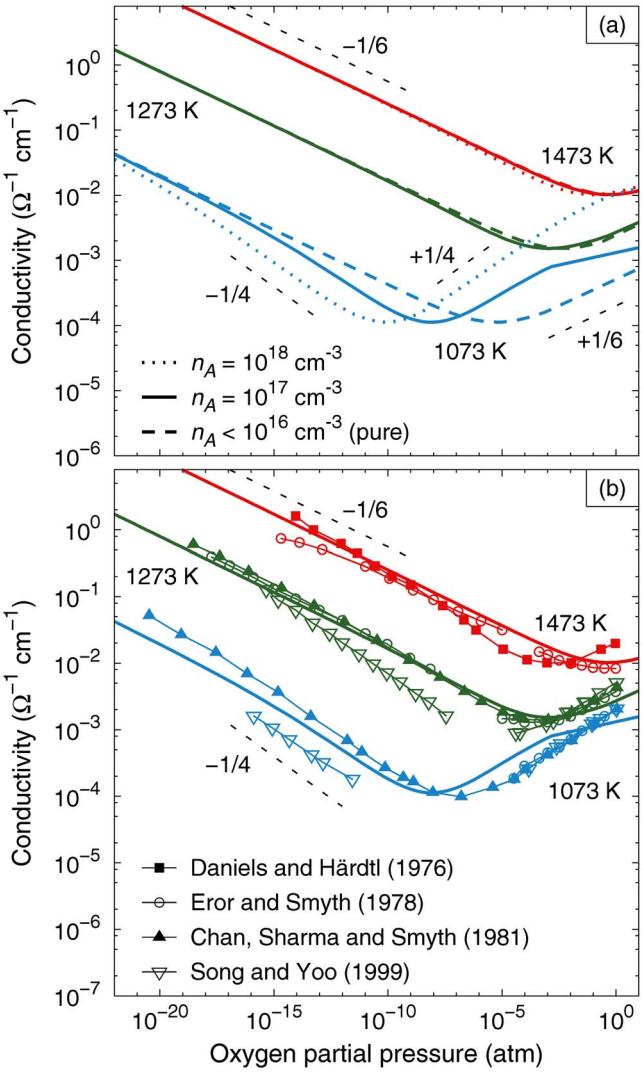


FIG. 2. (Color online) (a) Calculated conductivity as a function of oxygen chemical potential along the line A–D (i.e., for barium-rich conditions) in Fig. 1. The results in the absence of any impurities $n_A=0$ cm$^{-3}$ are shown by dotted lines; solid and dashed lines correspond to acceptor doping levels of $n_A=10^{17}$ cm$^{-3}$ and $n_A=10^{18}$ cm$^{-3}$, respectively. (b) Comparison of calculated (thick solid lines) and experimentally measured conductivity curves (thin lines and symbols). Experimental data from Refs. 15–18. For the calculations in (b) an accidental acceptor doping level of $n_A=10^{17}$ cm$^{-3}$ was adopted.

$$\mu_O(T,p_{O_2}) = \mu_O(T,p^0) + \frac{1}{2}k_BT\ln\left(\frac{p_{O_2}}{p^0}\right), \tag{16}$$

where $p^0_{O_2}$ denotes the reference pressure. We choose the isolated oxygen dimer molecule as the 0 K reference state, $\mu^0_O(0\ \mathrm{K},p^0)=\frac{1}{2}E_{O_2}$. For consistency with the experimental data and following Ref. 28 we use the experimental value for $E_{O_2}=-5.16$ eV/dimer and the experimentally determined temperature dependence of $\mu_O(T,p^0_{O_2})$ (Ref. 30).

The phase diagram in Fig. 1 is strictly valid only at zero temperature. At finite temperatures the construction would have to be based on the free energies of formation instead. The major effect arises from the differences between the vibrational entropies between the various relevant phases. With the exception of oxygen all these phases are crystalline. The entropies of crystalline solids are, however, much smaller than the entropies of gases. By the far the most important term is therefore the change of the free energy of the oxygen reservoir, which is properly taken into account via Eq. (16). It is therefore admissible to use the phase diagram established here also at finite temperatures.

### E. Summary of algorithm

In summary computing the conductivity proceeds as follows: (i) The electron chemical potential is self-consistently determined as described in Sec. II B for a fixed set of atomic chemical potentials (see Sec. II D). (ii) The concentrations of the intrinsic charge carriers and the intrinsic defects are evaluated using Eqs. (5a), (5b), (6a), and (6b). (iii) The conductivity is calculated as described in Sec. II C and the oxygen chemical potential is converted to an oxygen partial pressure according to Eq. (16). In the following we explicitly assume that the material is always able to reach equilibrium, which is a reasonable assumption at elevated temperatures. Further computational details are given in the Appendix.

## III. RESULTS AND DISCUSSION

### A. Equilibrium conductivity at elevated temperatures

We have implemented the model described earlier and used the formation energies from Ref. 8. A band gap of $E_G=3.0$ eV was employed which is 0.4 eV smaller than the 0 K-extrapolated band gap mimicking the shrinking of the band gap with increasing temperature. The value of 3.0 eV lies between the value obtained by temperature scaling of the band gap reported by Wemple,[31] which yields approximately 2.8 eV at 1400 K, and the values for the band gap discussed by Chan *et al.*,[17] which range between 3.0 and 3.4 eV. Both undoped and weakly ("accidentally") doped materials ($n_A^{ext}=10^{17}$ cm$^{-3}$ and $10^{18}$ cm$^{-3}$) were considered. The calculated equilibrium conductivity as a function of temperature, impurity concentration, and oxygen partial pressure is shown in Fig. 2. All curves display the shape characteristic for a transition from *n*-type (negative slope) to *p*-type (positive slope) conduction.

#### *1. Undoped material*

First we consider an ideally pure material ($n_A^{ext}=0$ cm$^{-3}$) under Ba-rich conditions (i.e., for chemical potentials along A–D in Fig. 1) for which the thin dotted lines in Fig. 2 are obtained. Throughout the *n*-type region a slope of $-1/6$ is observed [compare the dashed line segments in Fig. 2(a)], which changes to $+1/6$ in the *p*-type region. Analysis of the defect concentrations [Fig. 3(a)] shows that in the *n*-type region doubly charged oxygen vacancies are the dominant defects which gives rise to a slope of $-1/6$. This slope can also be derived if one treats the point defect equilibria in the material using the mass-action law approach.[17,32] Starting from the point defect reaction

$$O_O \leftrightarrow V_O^{\cdot\cdot} + 2e' + \frac{1}{2}O_2,$$

one obtains a mass-action law which links the oxygen partial pressure, $p_{O_2}$, to the concentration of doubly charged oxygen

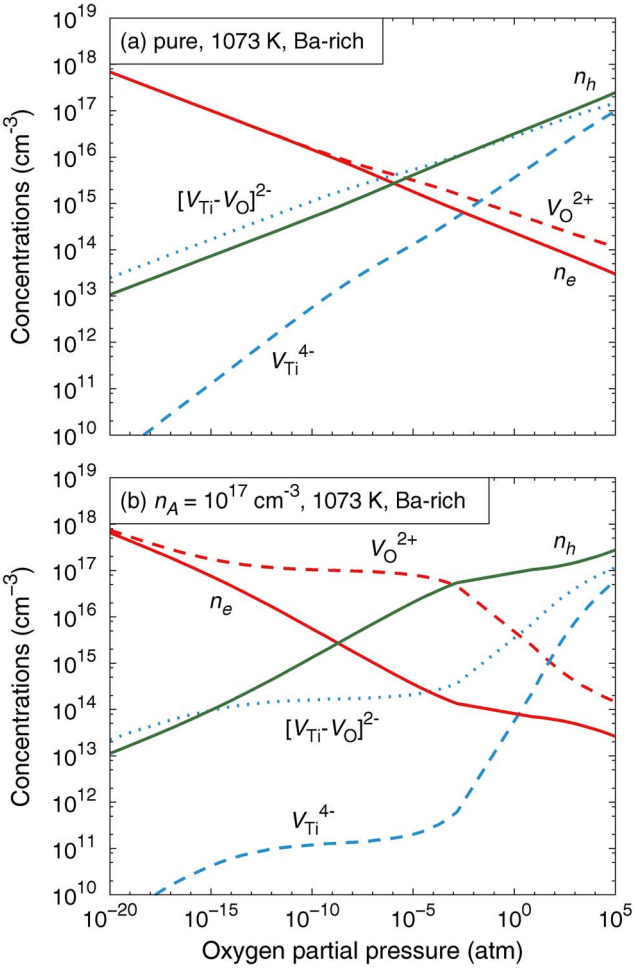


FIG. 3. (Color online) Charge carrier and defect concentrations for (a) pure and (b) accidentally acceptor doped material ($n_A^{\mathrm{ext}}=10^{17}$ cm$^{-3}$).

vacancies, $[V_O^{\cdot\cdot}]$, and the concentration of electrons, $n_e$,

$$K_I = [V_O^{\cdot\cdot}] n_e^2 p_{O_2}^{1/2}. \tag{17}$$

Application of the Brouwer approximation [one defect dominates the charge neutrality condition, Eq. (4)] for the oxygen vacancies $[V_O^{\cdot\cdot}]=2n_e$ then yields

$$n_e \propto p_{O_2}^{-1/6}, \tag{18}$$

which because of Eq. (11) leads to the same slope in the conductivity.

In the $p$-type region $(V_{Ti}-V_O)''$ divacancies dominate, leading to a slope of $+1/6$. The latter can be derived using the mass-action law approach as follows. The point defect reaction

$$\mathrm{BaO} + \frac{1}{2}\mathrm{O}_2 \leftrightarrow (V_{Ti} - V_O)'' + 2h^{\cdot} + \mathrm{BaTiO}_3$$

leads to

$$K_{II} = [(V_{Ti} - V_O)''] n_h^2 p_{O_2}^{-1/2}, \tag{19}$$

which using the simplified charge neutrality condition $[(V_{Ti}-V_O)'']=2n_h$ yields

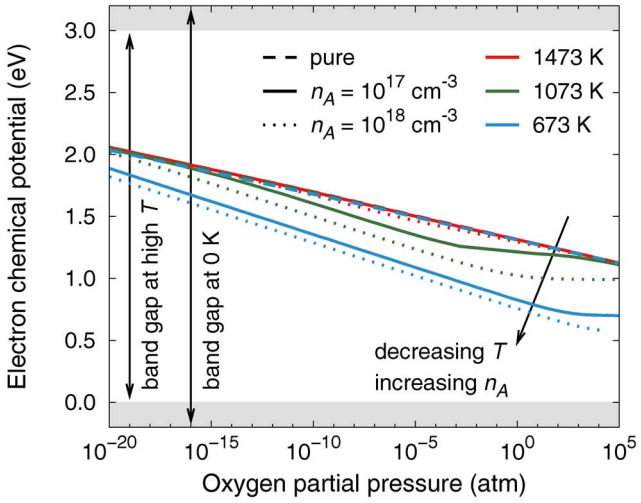


FIG. 4. (Color online) Variation of the electron chemical potential with both temperature and impurity concentration. The curves move downward, i.e., to more $p$-type conditions, with decreasing temperature as well as increasing impurity concentrations. The gray bars indicate the reduction of the band gap at higher temperatures.

$$n_h \propto p_{O_2}^{+1/6}. \tag{20}$$

For clarification it should be pointed out that if the conductivity is plotted not against the oxygen partial pressure but against the oxygen chemical potential the minima all occur at the same chemical potential. The gradual shift of the minima in Fig. 2 is thus merely a consequence of the temperature dependence of the relation between the chemical potential and the oxygen partial pressure described by Eq. (16).

The self-consistently determined electron chemical potential is shown in Fig. 4. At low oxygen partial pressures it is located in the upper half of the band gap corresponding to $n$-type material whereas for larger oxygen partial pressures the electron chemical potential resides in the lower half of the band gap. Figure 4 shows that for an ideally pure material the pressure dependence of the electron chemical potential does not change with temperature. This observation contrasts with the temperature induced shift of the minimum of the conductivity curves [Fig. 2(a)].

The temperature and pressure dependence of the conductivity as well as the electron chemical potential obtained under Ti-rich conditions (i.e., for chemical potentials along the line B–C in Fig. 1) very closely resemble the results under Ba-rich conditions. In the $n$-type region doubly charged oxygen vacancies are again the primary defects. In the $p$-type region, however, doubly charged barium vacancies dominate. Following a similar derivation as for the $V_{Ti}-V_O$ divacancies (see e.g., Ref. 17) one again obtains a slope of $+1/6$.

As demonstrated earlier the use of the mass-action law and the Brouwer approximation allow one to deduce the slope of the curves for situations in which one defect dominates. Such an approach is, however, bound to fail in any transition region or in regions where several point defects have similar concentrations. This is, for example, the case near the crossings of the lines in Fig. 3. This limitation is avoided by using the full approach outlined in Sec. II which furthermore does not require any presumptions with regard

to the prevalence of any particular defect reaction. In addition it allows one to obtain the concentrations of secondary point defects which although they do not affect the charge carrier concentrations still can impact the electronic properties through carrier scattering and trapping.

#### 2. Weakly acceptor doped material

If under Ba-rich conditions a low concentration of acceptors is present in the material, one obtains the bold solid lines in Fig. 2 ($n_A^{\mathrm{ext}}=10^{17}$ cm$^{-3}$). For low oxygen partial pressures and high temperatures they have a slope of $-1/6$ in the $n$-type region just as in the undoped material. Again this is due to positively charged oxygen vacancies as illustrated in Fig. 3(b). As the temperature is lowered and/or the oxygen partial pressure rises, a transition to a slope of $-1/4$ is observed. As shown in Fig. 3(b) this change corresponds to the onset of extrinsic behavior, i.e., the dominant source for holes are no longer intrinsic but extrinsic defects. In this case the simplified charge neutrality condition reads $[V_{\mathrm{O}}^{\cdot\cdot}]=2n_A^{\mathrm{ext}}$ which if inserted into Eq. (17) also leads to a slope of $+1/4$. At higher oxygen partial pressures and higher temperatures the slope changes to $+1/6$—as in the ideal case—indicating intrinsic behavior and dominance of $V_{\mathrm{Ti}}-V_{\mathrm{O}}$ divacancies. In contrast, at lower temperatures a slope of $+1/4$ is observed which is consistent with extrinsic behavior.[17]

As shown in Fig. 4 the electron chemical potential as a function of the oxygen partial pressure again displays a reduction of the slope for pressures $\gtrsim 10^{-3}$ atm which results from the coupling of the concentrations of intrinsic holes and extrinsic defects which are of similar magnitude in this range. For even larger oxygen partial pressures [outside the range of Fig. 2 but visible in Fig. 3(b)], the concentration of $V_{\mathrm{Ti}}-V_{\mathrm{O}}$ divacancies exceeds the concentration of extrinsic acceptors and the slope of the conductivity curves reverts to $+1/6$. The transition from $n$-type to $p$-type conduction correlates with a significant variation of the electron chemical potential over the band gap. In contrast to the case of an ideally pure material, material which contains extrinsic defects exhibits a marked temperature dependence of the electron chemical potential versus pressure curves. As the temperature is reduced the electron chemical potential curves are pushed downwards, which leads to the remarkable finding that for a certain range of oxygen partial pressures, the electron chemical potential moves from the upper to the lower half of the band gap as the temperature is lowered, indicating a transition from $n$- to $p$-type conduction.

If the dopant concentration is further raised (thin dotted lines in Fig. 2, $n_A^{\mathrm{ext}}=10^{18}$ cm$^{-3}$) extrinsic acceptors dominate over the entire range of chemical potentials and a slope of $-1/4$ ($+1/4$) is obtained throughout the $n$-type ($p$-type) region. The temperature dependence of the electron chemical potential curves (Fig. 4) is even more pronounced than in the case of $n_A^{\mathrm{ext}}=10^{17}$ cm$^{-3}$.

The entire situation is very similar if Ti-rich conditions are imposed, the major difference being again the occurrence of barium vacancies instead of $V_{\mathrm{Ti}}-V_{\mathrm{O}}$ divacancies in the $p$-type region.

### B. Comparison with experiment

The conductivity of both nominally undoped as well as intentionally doped barium titanate has been repeatedly measured as a function of oxygen partial pressure and at elevated temperatures.[11,15–18,33,34] These studies provide a comprehensive data set for comparing our calculations with experiment. In Fig. 2(b) the results of several measurements are plotted together with the curves calculated for a doping level of $n_A^{\mathrm{ext}}=10^{17}$ cm$^{-3}$. The agreement is very good. The calculations reproduce the $n$-type/$p$-type transition, the temperature dependence of the position of the minima, as well as the changes in the slopes.

In order to explain the experimentally observed transition within the $n$-type region from a slope of $-1/6$ to a slope of $-1/4$, two different models have been discussed: (i) The most early studies proposed the transition to be related to a change of the charge state of the oxygen vacancy.[15] The measurements could be reproduced using a model in which the oxygen vacancy $+1/+2$ transition level is located about 1.3 eV below the CBM and thus very close to the center of the band gap. (ii) Most studies (see e.g., Refs. 16, 17, 34, and 35), however, assume that even in the most carefully prepared samples a background concentration of "accidental" acceptor impurities is present which gives rise to the transition between the slopes.

The present calculations in conjunction with the DFT data from Ref. 8 provide very strong evidence for the second explanation. In order to obtain further support for this picture, we artificially pushed the $+2/+1$ transition level, which is located just 0.05 eV below the conduction band minimum, toward the middle of the band gap by reducing the formation energy of the singly charged oxygen vacancy. Thus the obtained conductivity curves do indeed display a transition from $\sigma\propto p_{\mathrm{O}_2}^{-1/6}$ to $\sigma\propto p_{\mathrm{O}_2}^{-1/4}$. However, in order to reproduce at least approximately the experimental data the formation energy of $V_{\mathrm{O}}$ had to be reduced by about 1 eV, which is significantly larger than the error bar of the DFT calculations.

The $p$-type region within which the slope is positive is dominated by acceptor defects. Since experimentally one observes a slope of about $+1/6$ in this region, it has been widely assumed that barium vacancies in charge state $-2$ are responsible for this behavior. If one considers single vacancies only the alternative intrinsic acceptor defect would be the titanium vacancy, which occurs in charge state $-4$ and thus would lead to a slope of $+1/5$. The earlier discussion, however, shows that at least under Ba-rich conditions the dominant defect is the $V_{\mathrm{Ti}}-V_{\mathrm{O}}$ divacancy, which—equivalent to the barium vacancy—gives rise to a slope of $+1/6$. Thus, on the basis of the conductivity curves alone the intrinsic acceptor defect cannot be determined unambiguously.

### C. Equilibrium defect concentrations

The validation of our calculations through comparison with experimental data demonstrates the capacity of DFT calculations and allows one to use the present calculations for obtaining a more detailed picture of the thermodynamical behavior of point defects in this material. We can thus deter-

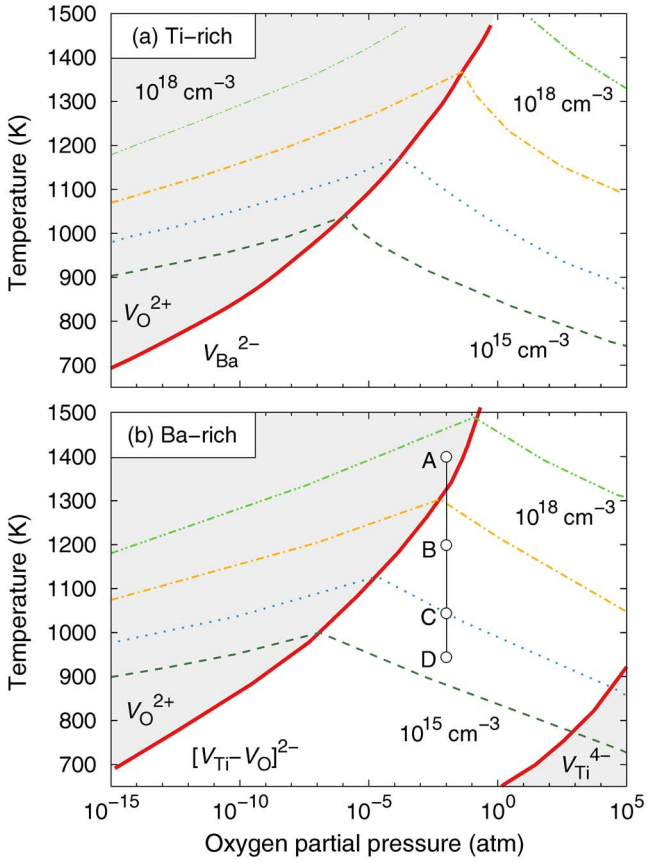


FIG. 5. (Color online) Phase diagram illustrating the prevalent defects as a function of temperature and oxygen partial temperature. The thick solid lines separate the regions within which the indicated defects dominate. The dotted and dashed lines connect points along which the concentration of the dominant defect is constant (dash-dot-dot: $10^{18}$ cm$^{-3}$, dash-dot: $10^{17}$ cm$^{-3}$, dotted: $10^{16}$ cm$^{-3}$, dashed: $10^{15}$ cm$^{-3}$).

mine the prevalent intrinsic point defects depending on temperature and oxygen partial pressure. The results obtained for an ideally pure material are shown for Ba- and Ti-rich conditions in Fig. 5. In this figure thick solid lines confine the regions within which a certain defect prevails. The concentration of the dominant defects is shown by the dashed lines along which the concentration is constant.

The diagrams can be read as follows: Assume a material is synthesized at 1400 K under Ba-rich conditions and an oxygen partial pressure of $10^{-2}$ atm [point A in Fig. 5(b)]. The material contains an acceptor impurity concentration of $10^{16}$ cm$^{-3}$. Under the synthesis conditions the dominant defect is the oxygen vacancy in charge state +2. The material is subsequently annealed at a temperature of 1200 K while keeping the oxygen partial pressure at $10^{-2}$ atm [point B in Fig. 5(b)]. Under these conditions the dominant defect is the $V_{Ti}-V_O$ divacancy. If the material is cooled below about 1000 K, the dotted line in Fig. 5(b) indicates that the concentration of $V_{Ti}-V_O$ divacancies falls below $10^{16}$ cm$^{-3}$ [point C in Fig. 5(b)]. Therefore, at temperatures below 1000 K, the accidental acceptor dopants dominate the charge equilibrium and the material displays extrinsic behavior [point D in Fig. 5(b)]. It is important to point out that this analysis is strictly valid only in thermodynamic equilibrium.

## IV. SUMMARY AND CONCLUSIONS

By combining thermodynamic considerations and several basic relations of semiconductor physics we have obtained a concise scheme for the modeling of electrical conductivities on the basis of first-principles calculations. Compared to "classical" defect models which are based on mass-action laws to connect defect concentrations, the present scheme requires a minimum number of approximations. In particular, it does not rely on any assumptions with regard to the prevalence of any particular defect reaction or defect.

We have applied this scheme to $BaTiO_3$, which is important both from the technological and the fundamental perspective, using a complete set of thermodynamic data on intrinsic point defects obtained from density-functional theory calculations. A numerical algorithm was implemented for the self-consistent determination of the electron chemical potential, which enabled an extensive analysis of the dependence of the electrical conductivity on chemical environment as well as temperature.

In agreement with earlier experimental studies our analysis has shown that the *n*-type conductivity, which is observed under low oxygen partial pressures, is due to doubly charged oxygen vacancies. The *p*-type region, which is observed at larger oxygen partial pressure, is caused by barium vacancies and $V_{Ti}-V_O$ divacancies under Ti- and Ba-rich conditions, respectively. It needs to be stressed that since both of these defects occur in charge state −2 and therefore lead to a slope of +1/6 in the conductivity versus oxygen partial pressure plot, they cannot be distinguished on the basis of the conductivity curves alone.

Our approach furthermore allows us to determine the evolution of the defect concentrations under "true" equilibrium conditions, i.e., in the absence of any kinetic barriers. We have employed this possibility to establish a point defect "phase diagram" which displays the dominant intrinsic point defect as a function of temperature and chemical environment.

The application of the scheme outlined in the present paper demonstrates the predictive power of first-principles calculations. It also constitutes the stepping stone for future work which should address the effects of kinetic barriers and implement a more complex treatment of extrinsic defects.

## ACKNOWLEDGMENTS

This project was funded by the Sonderforschungsbereich 595 "Fatigue in functional materials" of the Deutsche Forschungsgemeinschaft.

## APPENDIX: COMPUTATIONAL DETAILS

### 1. General remarks

The DFT calculations[8] from which we obtain our input data provide values for the energies of formation $E_i$. (The formation energies given in Ref. 8 have been subjected to a finite-size scaling procedure which has been shown in Ref. 7 to be equivalent to extrapolation to zero external pressure.)

In order to obtain the free energies of formation $\Delta G_i^f$ the (vibrational) entropies of formation $\Delta S_i^f$ and the formation volumes $\Delta V_i^f$ are required,

$$\Delta G_i^f = E_i^f - T\Delta S_i^f + p\Delta V_i^f. \quad \text{(A1)}$$

Since we are interested in ambient pressures (i.e., $p \approx 0$) the last term is virtually zero. It is in principle possible to determine the vibrational entropy but it requires very large supercells, which is computationally extremely demanding.[37] In the present work we, therefore, simply set all defect formation entropies to $\frac{3}{2}k_B$ which at 1200 K amounts to a reduction of the free energy of formation by 0.16 eV compared to the 0 K value.

### 2. Effect of band gap corrections

The formation energies in Ref. 8 were calculated within density functional theory using the local density approximation. Since this calculation method is subject to a substantial band gap underestimation, a correction scheme was applied which implements a rigid shift of the conduction versus the valence band states. In simple terms, the difference between the experimental $E_G^{\text{exp}}$ and the calculated band gap $E_G^{\text{calc}}$ is distributed between the valence and the conduction band states,

$$\Delta E_G^{\text{err}} = E_G^{\text{exp}} - E_G^{\text{calc}} = \Delta E_{\text{VB}} + \Delta E_{\text{CB}}. \quad \text{(A2)}$$

Unfortunately, the ratio of $\Delta E_{\text{VB}}$ and $\Delta E_{\text{CB}}$ is unknown. Even the *GW* method,[36] which in principle is capable of providing this information and which works well for many nonoxide materials, fails and yields a considerable overestimation of the band gap.[5] In Ref. 8 we therefore simply assigned the band gap error entirely to the conduction band, $\Delta E_{\text{CB}} = \Delta E_G^{\text{err}}$, $\Delta E_{\text{VB}} = 0$. This choice has neither an impact on the location of the equilibrium transition levels nor on the conclusions in Ref. 8. The values of $\Delta E_{\text{VB}}$ and $\Delta E_{\text{CB}}$ do, however, affect the absolute values of the formation energies and are therefore important in the present work.

By explicit calculation one can show that the effect of shifting $\Delta E_{\text{VB}}$ versus $\Delta E_{\text{CB}}$ is equivalent to rigidly shifting the conductivity curves in Fig. 2 (details later) along the pressure axis. Neither the shape, the slopes, nor the magnitude of these curves are affected. We have therefore decided to adjust the ratio of $\Delta E_{\text{VB}}$ and $\Delta E_{\text{CB}}$ such that the minimum of the conductivity at the highest temperature considered (1473 K) is located at the same oxygen partial pressure as in the experiments. The final values are $\Delta E_{\text{VB}} = 0.45\Delta E_G^{\text{err}} = 0.76$ eV and $\Delta E_{\text{CB}} = 0.55\Delta E_G^{\text{err}} = 0.92$ eV, which are actually of a very reasonable magnitude, considering that a rule of thumb for many semiconductors is a ratio of 2:1 for $\Delta E_{\text{CB}} : \Delta E_{\text{VB}}$. A shift of 0.1 eV in either direction amounts to a shift in along the pressure axis by $10^{\pm 2}$ atm. All data discussed in the following were obtained using the values for $\Delta E_{\text{VB}}$ and $\Delta E_{\text{CB}}$ quoted before.


[1] R. A. Eichel, P. Erhart, P. Träskelin, K. Albe, H. Kungl, and M. J. Hoffmann, Phys. Rev. Lett. **100**, 095504 (2008).
[2] R. A. Eichel, J. Am. Ceram. Soc. **91**, 691 (2008).
[3] S. Gottschalk, H. Hahn, A. G. Balogh, W. Puff, H. Kungl, and M. J. Hoffmann, J. Appl. Phys. **96**, 7464 (2004).
[4] A. R. Allnatt and A. B. Lidiard, *Atomic Transport in Solids* (Cambridge University Press, Cambridge, 2003).
[5] E. Rauls and T. Frauenheim, Phys. Rev. B **69**, 155213 (2004).
[6] S. A. Centoni, B. Sadigh, G. H. Gilmer, T. J. Lenosky, T. Diaz de la Rubia, and C. B. Musgrave, Phys. Rev. B **72**, 195206 (2005).
[7] P. Erhart, K. Albe, and A. Klein, Phys. Rev. B **73**, 205203 (2006).
[8] P. Erhart and K. Albe, J. Appl. Phys. **102**, 084111 (2007).
[9] P. Erhart and K. Albe, Phys. Rev. B **73**, 115207 (2006).
[10] P. Erhart and K. Albe, Appl. Phys. Lett. **88**, 201918 (2006).
[11] D. M. Smyth, *The Defect Chemistry of Metal Oxides* (Oxford University Press, New York, 2000), Chap. 14.
[12] M. Fukunaga, G. Li, Y. Uesu, and K. Kohn, Ferroelectrics **286**, 79 (2003).
[13] A. Tombak, J. P. Maria, F. Ayguavives, Z. Jin, G. T. Stauf, A. I. Kingon, and A. Mortazawi, IEEE Microw. Wirel. Compon. Lett. **12**, 3 (2002).
[14] A. Feteira, D. C. Sinclair, I. M. Reaney, Y. Somiya, and M. T. Lanagan, J. Am. Ceram. Soc. **87**, 1082 (2004).
[15] J. Daniels and K. H. Härdtl, Philips Res. Rep. **31**, 489 (1976).
[16] N. G. Eror and D. M. Smyth, J. Solid State Chem. **24**, 235 (1978).
[17] N. H. Chan, R. K. Sharma, and D. M. Smyth, J. Am. Ceram. Soc. **64**, 556 (1981).
[18] C.-R. Song and H.-I. Yoo, Solid State Ionics **120**, 141 (1999).
[19] F. D. Morrison, D. C. Sinclair, and A. R. West, J. Appl. Phys. **86**, 6355 (1999).
[20] S. H. Yoon, K. H. Lee, and H. Kim, J. Am. Ceram. Soc. **83**, 2463 (2000).
[21] F. D. Morrison, D. C. Sinclair, and A. R. West, J. Am. Ceram. Soc. **84**, 531 (2001).
[22] E. J. Lee, J. Jeong, and Y. H. Han, Jpn. J. Appl. Phys., Part 1 **43**, 8126 (2004).
[23] H. Beltran, E. Cordoncillo, P. Escribano, D. C. Sinclair, and A. R. West, J. Appl. Phys. **98**, 094102 (2005).
[24] G.-X. Qian, R. M. Martin, and D. J. Chadi, Phys. Rev. B **38**, 7649 (1988).
[25] S. B. Zhang, S.-H. Wei, and A. Zunger, Phys. Rev. Lett. **84**, 1232 (2000).
[26] H. Ihrig, J. Phys. C **9**, 3469 (1976).
[27] P. Ghosez, X. Gonze, and J. P. Michenaud, Ferroelectrics **194**, 39 (1997).
[28] K. Reuter and M. Scheffler, Phys. Rev. B **65**, 035406 (2001).
[29] W. Zhang, J. R. Smith, and X.-G. Wang, Phys. Rev. B **70**, 024103 (2004).
[30] M. W. Chase, Jr., *JANAF Thermochemical Tables*, 4th ed. (Springer, New York, 1998).
[31] S. H. Wemple, Phys. Rev. B **2**, 2679 (1970).
[32] J. Maier, *Physical Chemistry of Ionic Materials* (Wiley, New York, 2004).
[33] N. H. Chan, R. K. Sharma, and D. M. Smyth, J. Am. Ceram. Soc. **65**, 167 (1982).
[34] N. H. Chan and D. M. Smyth, J. Am. Ceram. Soc. **67**, 285 (1984).
[35] H. I. Yoo, C. R. Song, and D. K. Lee, J. Electroceram. **8**, 5 (2002).
[36] W. G. Aulbur, L. Jönsson, and J. W. Wilkins, Solid State Phys. **54**, 1 (2000).
[37] P. Erhart (unpublished).